

Activating Peroxymonosulfate Using Carbon from Cyanobacteria as Support for Zero-Valent Iron

Jun Chen (✉ chenjun@hfuu.edu.cn)

Hefei University

Layun Zhu

Hefei University

Sisi Cao

Hefei University

Zhaoming Chen

Hefei University

Zihui Song

Hefei University

Xiaohong Yang

Hefei University

Jie Jin

Hefei University

Research Article

Keywords: Cyanobacterial carbon, NZVI@ACC, PMS activation

Posted Date: January 18th, 2022

DOI: <https://doi.org/10.21203/rs.3.rs-1042547/v1>

License:  This work is licensed under a Creative Commons Attribution 4.0 International License.

[Read Full License](#)

1 **Activating Peroxymonosulfate using Carbon from Cyanobacteria as**
2 **Support for Zero-valent Iron**

3 **Jun Chen**^{a,b}

4 Corresponding author. Tel.: +86 551 62158405; Fax: +86 551 62158406.

5 E-mail: chenjun@hfu.edu.cn

6 ^a *School of Biology, Food and Environment, Hefei University, Hefei 230601, P. R. China.*

7 ^b *Anhui Key Laboratory of Sewage Purification and Eco-restoration Materials, Hefei 230088, P.*
8 *R. China.*

9 **Layun Zhu**^{a,b}

10 ^a *School of Biology, Food and Environment, Hefei University, Hefei 230601, P. R. China.*

11 ^b *Anhui Key Laboratory of Sewage Purification and Eco-restoration Materials, Hefei 230088, P.*
12 *R. China.*

13 **Sisi Cao**^{a,b}

14 ^a *School of Biology, Food and Environment, Hefei University, Hefei 230601, P. R. China.*

15 ^b *Anhui Key Laboratory of Sewage Purification and Eco-restoration Materials, Hefei 230088, P.*
16 *R. China.*

17 **Zhaoming Chen**^{a,b}

18 ^a *School of Biology, Food and Environment, Hefei University, Hefei 230601, P. R. China.*

19 ^b *Anhui Key Laboratory of Sewage Purification and Eco-restoration Materials, Hefei 230088, P.*
20 *R. China.*

21 **Zihui Song**^{a,b}

22 ^a *School of Biology, Food and Environment, Hefei University, Hefei 230601, P. R. China.*

23 ^b *Anhui Key Laboratory of Sewage Purification and Eco-restoration Materials, Hefei 230088, P.*
24 *R. China.*

25 **Xiaohong Yang**^{a,b}

26 ^a *School of Biology, Food and Environment, Hefei University, Hefei 230601, P. R. China.*

27 ^b *Anhui Key Laboratory of Sewage Purification and Eco-restoration Materials, Hefei 230088, P.*
28 *R. China.*

29 **Jie Jin**^{a,b}

30 ^a *School of Biology, Food and Environment, Hefei University, Hefei 230601, P. R. China.*

31 ^b *Anhui Key Laboratory of Sewage Purification and Eco-restoration Materials, Hefei 230088, P.*
32 *R. China.*

33

34

35

36 **Activating Peroxymonosulfate using Carbon from Cyanobacteria as**
37 **Support for Zero-valent Iron**

38 Jun Chen^{a,b,*}, Layun Zhu^{a,b}, Sisi Cao^{a,b}, Zhaoming Chen^{a,b}, Zihui Song^{a,b}, Xiaohong
39 Yang^{a,b}, Jie Jin^{a,b}

40 ^a School of Biology, Food and Environment, Hefei University, Hefei 230601, P. R. China.

41 ^b Anhui Key Laboratory of Sewage Purification and Eco-restoration Materials, Hefei 230088, P.
42 R. China.

43

44 **Abstract**

45 In the present study, the cyanobacterial char (ACC) prepared from Chaohu
46 cyanobacteria was used as a nanoscale carrier for zero-valent iron (NZVI) to
47 synthesize a highly efficient activation material designated as cyanobacterial char-
48 supported nanoscale zero-valent iron (NZVI@ACC), which was subsequently used
49 for activating peroxydisulfate (PMS) to degrade the orange II (OII) dye. The XRD
50 and XPS results revealed that NZVI was anchored onto the ACC through
51 coordination bonding, thereby forming a stable structure. The SEM and TEM
52 observations revealed that the NZVI was embedded in the sheet structure of the ACC.
53 The NZVI@ACC had a larger specific surface area (42.249 m²/g), and also
54 magnetism, due to which its components could be separated through an externally
55 applied magnetic field. Using this NZVI@ACC/PMS system, the rate of degradation
56 of OII (100 mg/L) reached 98.32% within 14 min. The OII degradation reaction using
57 the NZVI@ACC/PMS system followed first-order kinetics. The activation energy of
58 this degradation reaction was 17.34 kJ/(mol·K). Quenching and EPR experiments
59 revealed that both SO₄^{·-} and ·OH were produced in this reaction, with SO₄^{·-} playing
60 the major role in the reaction. The theoretical calculations revealed that SO₄^{·-} attacked
61 the 12 (N) of OII, which destroyed and degraded the structure of OII. The presence of
62 halogen ions in the actual dye-containing wastewater samples inhibited the OII
63 degradation by the NZVI@ACC system to different degrees, and the inhibition effect
64 followed the order: I⁻ > Br⁻ > Cl⁻.

65 **Keywords:** Cyanobacterial carbon; NZVI@ACC; PMS activation

* Corresponding author. Tel.: +86 551 62158405; Fax: +86 551 62158406.

E-mail: chenjun@hfu.edu.cn

66 1. Introduction

67 Advanced oxidation processes (AOPs) based on sulfate radicals are gaining
68 increasing attention recently. In comparison to the hydroxyl radical ($\cdot\text{OH}$)-based
69 advanced oxidation, the sulfate radical ($\text{SO}_4\cdot^-$)-based AOPs have a higher redox
70 potential (2.5 ~ 3.1 V) and a longer half-life [$T_{1/2}(\text{SO}_4\cdot^-) = 30 \sim 40 \mu\text{s}$; $T_{1/2}(\cdot\text{OH}) = 10^{-3}$
71 μs], which becomes a contributing factor in the effective and sustainable degradation
72 of refractory organic matter in water (Yang, et al.2011; Sun, et al. 2019). In a typical
73 AOP, peroxymonosulfate (PMS) may be activated to generate $\text{SO}_4\cdot^-$ using various
74 activation methods, including those based on the ultraviolet light, electricity, heat,
75 alkali, and transition metal ions such as Cu^{2+} , Co^{2+} , Fe^{2+} , etc. (Wang, et al., 2017; Sun,
76 et al., 2017; Xu, et al., 2020). Light-based and thermal activation methods are
77 expensive and energy-consuming, rendering it difficult to achieve effective PMS
78 activation in dark and low-temperature environments. Moreover, the commonly
79 available transition metals, such as Ag^+ , Co^{2+} , and Cu^{2+} , are biotoxic and prone to
80 secondary pollution (Zha, et al., 2016; Czech, et al., 2015; Soubh, A., & Mokhtarani,
81 N. et al., 2016; Lin, Liang, Chen, et al., 2011).

82 Nanoscale zero-valent iron (NZVI), reduced iron powder, and other kinds of NZVI
83 have been used for catalyzing the PMS degradation of organic pollutants in the
84 environment. The term NZVI refers to the particles with sizes ranging from 1 to 100
85 nm, large specific surface area, and strong reducibility, properties that confer NZVI
86 with high reactivity and excellent adsorption performance. However, the small size
87 and the high reactivity of these nanoparticles leads to easy agglomeration, poor
88 dispersion, and no ideal reactivity, all of which seriously impact their performance
89 during the actual usage (Li, et al., 2019; Yan, et al., 2015). Therefore, various
90 methods for preventing agglomeration during practical application have been studied,
91 including the addition of a dispersant or carrier to the reaction system to disperse the
92 nanoparticles as they are synthesized (Zhong, et al., 2019; Song, et al., 2015).

93 With environment-friendly materials receiving increasing attention in the past few
94 years, environment-friendly carrier materials and biochar exhibiting ideal
95 immobilization and several economic and environmental advantages have gradually
96 emerged (Wu, et al., 2018; Lee, Gunten, Kim, 2020; Zhou, et al., 2014; Kwon, et al.,
97 2015). The phenomenon of eutrophication in several water bodies has caused
98 cyanobacteria to accumulate and occupy a large area of the water surface, leading to a

99 series of ecological and environmental problems, including infringing on livestock,
100 fish, and humans, and directly inducing liver cancer. The domestic measures for
101 cyanobacteria control are implemented mostly after the outbreak of water blooms.
102 The commonly used emergency control measures include salvage and ashore
103 treatment and disposal by manpower, ships, tools, or other physical methods.
104 However, disposal of algae sludge does not happen in time, thereby leading to various
105 environmental problems that are being now being focused on by the management
106 departments and all sectors of human society. Cyanobacteria are characterized by low
107 ash, high moisture, and high volatility, with levels of C, H, O, fixed carbon, and
108 volatility similar to those in rice straw and tung wood. These characteristics of
109 cyanobacteria allow their application in synthesizing materials with developed pore
110 structures (Zhang, et al., 2020; Gong, et al., 2017).

111 Meanwhile, researchers are also attempting to design and modify biochar using
112 various physical and chemical methods to further improve its performance. Since
113 different modification methods have different effects on biochar, it is particularly
114 important to improve the characteristics of biochar specific to the requirements (Lian,
115 et al., 2020; Ma, et al., 2018; Liu, et al., 2018).

116 In the present study, cyanobacterial char (ACC) supported nanoscale zero-valent
117 iron (NZVI@ACC) was prepared and then used for activating PMS to achieve the
118 removal of a typical refractory organic dye named OII from water samples. The study
119 included the following aspects: (1) characterization of the prepared NZVI@ACC, (2)
120 evaluation of the factors associated with the NZVI@ACC/PMS system influencing
121 the OII degradation, (3) determination of the active species of the reaction system and
122 analyzing the underlying activation mechanism, and (4) explore the effect of the
123 NZVI@ACC/PMS system on different halogens and dyes.

124 **2. Materials and Methods**

125 **2.1 Materials**

126 Cyanobacteria collected from Chaohu lake were used as the raw material for
127 obtaining biochar. PMS ($\text{KHSO}_5 \cdot 0.5\text{KHSO}_4 \cdot 0.5\text{K}_2\text{SO}_4$), $\text{FeSO}_4 \cdot 7\text{H}_2\text{O}$, NaBH_4 , HCl ,
128 NaOH , $\text{C}_2\text{H}_6\text{O}$, CH_3OH , $(\text{CH}_3)_3\text{COH}$, CH_4O (MeOH), and $\text{C}_4\text{H}_{10}\text{O}$ (TBA) were
129 purchased from Aladdin Reagent Co. Ltd. Congo red ($\text{C}_{32}\text{H}_{22}\text{N}_6\text{Na}_2\text{O}_6\text{S}_2$, CR),
130 methylene blue ($\text{C}_{18}\text{H}_{22}\text{ClN}_3\text{S}$, MB), and rhodamine B ($\text{C}_{28}\text{H}_{31}\text{ClN}_2\text{O}_3$, RB) were

131 purchased from Sinopharm Chemical Reagent Co. Ltd. All reagents used in the
132 present study were of analytical grade.

133 **2.2 Preparation of NZVI@ACC**

134 An appropriate amount of dry cyanobacteria powder was placed in a crucible. The
135 tube furnace was programmed to heat at 500 °C for 6 h at a heating rate of 10 °C/min
136 under N₂ protection. The carbonization temperature was maintained for the stated
137 duration and then the furnace was cooled. The carbonized powder was ground
138 through a 100-mesh sieve and then soaked in 1 mol/L of HCl for 12 h. After the
139 removal of ash, the powder was washed with deionized water, neutral dried, and
140 preserved. An amount of 3.754 g of FeSO₄·7H₂O was dissolved in 250 mL deionized
141 water (0.054 mol/L) followed by the addition of 250 mL of anhydrous ethanol as the
142 dispersant. ACC was added to this solution followed by magnetic stirring (200 r/min)
143 for 10 h. The solution was then dried and ground, and the obtained dry mixture was
144 dissolved in 100 mL of deoxidized and deionized water to obtain a solution.
145 Subsequently, intermediate products and 50 mL (1 ~ 2 drops/s) of 0.135 mol/L of
146 freshly prepared NaBH₄ solution were added to this solution under the protection of
147 nitrogen. After aging for 1 h, black particles were generated, which were first washed
148 three times with deoxidized and deionized water three times and then with ethanol.
149 Finally, after vacuum drying in an oven, NZVI@ACC was obtained and stored in a
150 sealed container for preservation.

151 **2.3 Experimental procedure**

152 The batch test was performed in a glass conical flask (250 mL) containing 100 mL
153 of the reaction solution. NZVI@ACC was added to 100 mL of OII (100 mg/L) at the
154 initial pH of 6. Subsequently, the flask was placed in an oscillation box at a constant
155 temperature of 25 °C and an oscillation frequency of 110 times/min. PMS (1 mmol/L)
156 was added and the duration was measured after dissolution. The effects of the
157 following parameters on the degradation of OII were studied: the dosage of
158 NZVI@ACC, the ratio of carbon to iron in NZVI@ACC, the reaction temperature,
159 and the reaction pH. At each measurement time point, a volume of 5 mL was sampled
160 and filtered through a 0.45 μm filter membrane. The absorbance of the filtered sample
161 was measured at 484 nm in an ultraviolet spectrophotometer.

162 **2.4 Analytical methods**

163 TD-3500 X-ray diffractometer (Dandong Tongda) was employed to radiate the
164 samples to obtain their X-ray diffraction (XRD) patterns. The XPS spectra were
165 obtained by scanning the samples using Thermo Fisher K-Alpha X-ray photoelectron
166 spectroscopic instrument (Thermo Field). In addition, the samples were gold-plated
167 and observed under an S-4800 cold-field emission scanning electron microscope
168 (Hitachi Company, Japan). Transmission electron microscopy (TEM) observation of
169 the samples was performed using FEI-TALOS-F200X. The free radicals in the
170 samples were detected using electron paramagnetic resonance (EPR, Bruker A300,
171 Germany). A vibrating sample magnetometer (VSM) was used at 7040 ± 2 T (Lake
172 Shore, American). The specific surface area and the pore size of the particles in the
173 sample were determined based on the nitrogen adsorption/desorption curves using a
174 fully automated surface and porosity tester (Quantachrome, USA).

175 **3. Results and Discussion**

176 **3.1 Material characterization**

177 **3.1.1 XRD and XPS analyses**

178 The XRD pattern and the results of the XPS survey, and XPS analysis of C 1s, O 1s,
179 and Fe 2p binding states in NZVI@ACC were depicted in Fig. 1. A sharp diffraction
180 peak was observed at 44.7° , as depicted in Fig. (a), while a weak diffraction peak was
181 observed at 64.8° . When compared to the standard PDF card (06-0696) of iron, these
182 two peaks corresponded precisely to the 110 crystal plane diffraction (44.7°) and 200
183 crystal plane diffraction (65.0°), respectively. According to Bragg's equation, the
184 crystal spacing was 0.203 nm. The chemical composition of NZVI@ACC was
185 revealed in the XPS analysis and was presented in Fig. 1 (b)-(e). The binding energies
186 of C 1s at 284.7 eV and 286.0 eV were classified as those of C-C and C-O,
187 respectively. In the Fe 2p spectra, the binding energy of the characteristic peaks at
188 707.00 eV, 710.70 eV, and 712.50 eV were attributed to Fe^0 , Fe^{2+} , and Fe^{3+} ,
189 respectively (Li, et al., 2019). After loading the NZVI onto NZVI@ACC, the Fe peak
190 [peak C depicted in Fig. 1 (c)] was formed at 288.7 eV, while the characteristic peak
191 of C-O exhibited a redshift [Fig. 1 (d)] indicating the loss of electrons of C and O
192 corresponding to the gain of electrons of Fe. According to the hybrid orbital theory, it
193 may be observed in Fig. 1(f), (g), and (h) that the lone pair electrons from C sp³ and
194 O sp³ hybrid orbital could occupy the Fe^{2+} sp³d² orbital, which suggests that a

195 coordinate bond (Fe-C and Fe-O) could be established between the NZVI and the
196 active group on the surface of ACC.

197 **3.1.2 SEM and TEM**

198 The morphology of the catalysts was observed using SEM and TEM. As depicted
199 in Fig. 2, the NZVI@ACC material had a loose structure and a flat lamellar
200 organization, which was attributed to the aggregation of NZVI during its formation
201 process. The TEM images were depicted in Fig. 2 (c, d). The TEM results revealed
202 that the iron particles (black spots in the depicted images) were highly dispersed
203 throughout ACC. The lattice spacing was determined to be 0.203 nm and the crystal
204 plane was (110). The images depicted in Fig. 2 (e, f) together confirmed the
205 successful preparation of NZVI@ACC with an even distribution of NZVI over the
206 ACC surface. However, although the prepared NZVI@ACC had an increased surface
207 area, it also contained an increased number of edges and defects.

208 **3.1.3 BET and Magnetic detection**

209 The Brunauer-Emmett-Teller (BET) surface area (S_{BET}) and the pore volume of
210 NZVI@ACC, determined according to the N_2 adsorption-desorption isotherm, and
211 BJH desorption pore size distribution were $49.249 \text{ m}^2/\text{g}$ and $0.104 \text{ cm}^3/\text{g}$, respectively
212 [Fig. 3 (a)]. According to the IUPAC classification, the adsorption isotherms of
213 NZVI@ACC were of the characteristic type IV, with P/P_0 having an H4 hysteresis
214 loop between 0.4 and 1.0. The prepared NZVI@ACC contained both micropores and
215 mesoporous pores, most with sizes of approximately 19.096 nm.

216 Fig. 3 (b) depicted the hysteresis loop of NZVI@ACC. The symmetric loop shape
217 of the origin indicated good ferromagnetism and sub-ferromagnetism of the prepared
218 NZVI@ACC, due to which its components could be separated using an external
219 magnetic field during a practical application thereby allowing material recycling. This
220 was also verified in experimental operation. The coercivity and magnetization of
221 NZVI@ACC were 233.16 Oe and 0.67 emu/g , respectively. The low saturation
222 magnetization of NZVI@ACC indicated that the particle size of NZVI@ACC was in
223 the micron range, which was consistent with the SEM results.

224 **3.2 Effects of reaction conditions on OII degradation**

225 The effects of activator dosage, Fe/C ratio, reaction temperature, and reaction pH
226 on the activation of PMS using NZVI@ACC were analyzed. The results were
227 presented in Fig. 4.

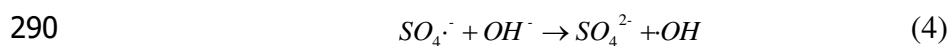
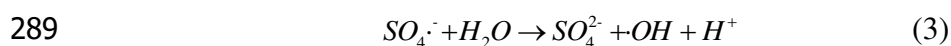
228 The effects of different dosages of activator on the degradation of OII were
229 presented in Fig. 4 (a) and Fig. 4 (e). Since NZVI@ACC provided the active sites, its
230 dosage affected the degradation effect of OII. PMS had a high redox potential (2.01
231 V), and due to its low activity, the rate of OII removal could only reach 4.62% within
232 14 min. When 0.1 g of NZVI@ACC was added to the system, the rate of OII removal
233 reached 98.32% within 14 min. With the increase in the dosage of NZVI, the oxygen-
234 containing functional groups on the surface of NZVI@ACC also increased, thereby
235 increasing the activation of PMS (Li, et al., 2016). The simulation results presented in
236 Fig. 4 (e) revealed that the reaction process conformed to first-order kinetics under the
237 influence of dosage. Within a certain range, both kinetic constant k and the reaction
238 rate increased. According to origin fitting analysis, the reaction rate constant
239 increased linearly with increasing dosage, which was consistent with $y = 2.89x -$
240 0.0108 ; the correlation index R^2 was 0.973. As the dosage increased, a greater
241 NZVI@ACC surface area was available for the reaction, which increased the reaction
242 rate. However, when the activator was in excess, no significant change was observed
243 in the effect of OII removal as the excessive activator led to wasted active sites and
244 decreased utilization rate of the material.

245 As visible in Fig. 4 (b), ACC had almost no catalytic effect on PMS, and the rate of
246 OII removal achieved using the ACC/PMS system was only 9.43% within 14 min.
247 After the addition of NZVI, which was a strong reducing agent, to the system, the OII
248 removal effect of the system was significantly improved. When the ratio of carbon to
249 iron in the NZVI@ACC/PMS system was 1:1, the OII removal rate reached 98.32%
250 within 14 min, which was almost complete removal. The NZVI@ACC/PMS system,
251 therefore, exhibited the best OII removal effect.

252 The influence of reaction temperature on the OII degradation effect was depicted in
253 Fig. 4 (c) and Fig. 4 (f). When the reaction temperature was 10 °C, the OII
254 degradation rate of 93.09% was reached within 14 min. When the reaction
255 temperature was increased to 25 °C and 40 °C, the OII removal rate increased to over
256 98.32%. It could be observed that within a certain range, an increase in the reaction
257 temperature could accelerate the molecular movement and improve the reaction speed.
258 Fig. 4 (f) illustrated the kinetic simulation of the OII degradation effects at different
259 temperatures, which conformed to quasi-first-order kinetics. The degradation rate
260 increased with the increase in the reaction temperature from 10 °C to 40 °C. The

261 increase in the temperature increased the energy absorbed by the molecules during the
 262 reaction and accelerated the decomposition to produce free radicals (Zrinyi, Pham,
 263 2017). Meanwhile, the molecular motion was accelerated, which increased the
 264 probability and the rate of molecular collision, thereby accelerating the reaction
 265 process (Hori, et al., 2005). According to the Arrhenius' law, the relationship between
 266 the reaction rate and the temperature followed the equation $\ln k = \ln A - E_a/RT$. After
 267 linear fitting $\ln k$ and $1/T$, the following fitting equation was obtained: $Y = -2086.2x +$
 268 5.7156 , and the activation energy of NZVI@ACC-activated PMS-based degradation
 269 of OII was calculated to be $17.34 \text{ kJ}/(\text{mol}\cdot\text{K})$.

270 Furthermore, the pH of the reaction system affects the free radicals in the system,
 271 which, in turn, has a significant influence on the PMS-based degradation of pollutants
 272 in wastewater. The results presented in Fig. 4 (d) revealed that at the initial reaction
 273 pH of 4, the OII removal rate was 99.01% within 14 min. At the pH of 6 and 8, the
 274 OII removal rates were 98.32% and 93.09%, respectively. Therefore, while a high
 275 degradation rate was maintained, the degradation rates were different at different pH
 276 values. In a weakly acidic environment, NZVI@ACC was more likely to precipitate
 277 Fe^{2+} , SO_4^{2-} , $\cdot\text{OH}$, and Fe^{3+} produced upon the activation of PMS by Fe^{2+} (equation 1
 278 and 2), thereby generating more $\cdot\text{OH}$ as $\text{SO}_4^{\cdot-}$ captured an electron from H_2O
 279 (equation 3) (Du, et al., 2016; Fuller, et al., 2013; Hussain, et al., 2017; Lin, et al.,
 280 2013). However, in alkaline conditions, $\text{SO}_4^{\cdot-}$ and OH^- could generate $\cdot\text{OH}$ with a
 281 slightly lower oxidation activity (equation 4), thereby decelerating the degradation
 282 rate, although the organic compounds could nonetheless be degraded by $\cdot\text{OH}$
 283 ultimately. When the pH increased to 10, the OII degradation rate of only 67.55%
 284 remained. With the increase of pH, a passivation layer was formed on the surface of
 285 NZVI, which inhibited the generation of free radicals, thereby decreasing the OII
 286 degradation rate (Gao, et al., 2019; Zhang, et al., 2020).



291 **3.4 Mechanism underlying the effect of OII degradation by NZVI@ACC-**
 292 **activated PMS**

293 MeOH reacts rapidly with both $\text{SO}_4^{\cdot-}$ (9.7×10^8 L/mol·s) and $\cdot\text{OH}$ (3.2×10^6
294 L/mol·s) (Huang, et al., 2014), TBA is well-recognized efficient scavenger of $\cdot\text{OH}$
295 that is not sensitive to $\text{SO}_4^{\cdot-}$ because of its higher reaction rate constant for $\cdot\text{OH}$ ($3.8 \sim$
296 7.6×10^8 L/mol·s) compared to that for $\text{SO}_4^{\cdot-}$ ($4.0 \sim 9.1 \times 10^5$ L/mol·s). Therefore,
297 TBA serves as the probe specifically for $\cdot\text{OH}$ (Pham, Suto, Inoue, 2009; Tsai, et al., 2008;
298 Anipsitakis, Dionysiou, 2004). The free radical inhibitors MeOH and TBA were
299 utilized to determine the contribution of $\text{SO}_4^{\cdot-}$ and $\cdot\text{OH}$ in the reaction process. The
300 results of the analysis were presented in Fig. 5 (a). An OII degradation rate of 98.32%
301 was achieved in the no scavenger group, which decreased to 74.54% and 84.49% after
302 the addition of MeOH and TBA, respectively. MeOH exhibited a greater inhibition
303 effect compared to TBA, based on which it was speculated that $\text{SO}_4^{\cdot-}$ played a major
304 role in the reaction. The free radicals generated in the NZVI@ACC/PMS system
305 remained concentrated on the surface of the activator and, therefore, the reaction
306 occurred on the surface of the activator (Dong, et al., 2019).

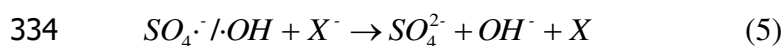
307 In order to determine the types of active free radicals generated in the reaction
308 process, the trapping agent DMPO was used for EPR detection during the degradation
309 process. The results were presented in Fig. 5 (b). No evident signal peak appeared for
310 the reaction system with only PMS, and the degradation rate achieved was only
311 4.62% without NZVI@ACC, which indicated that PMS was relatively stable and no
312 active free radicals were generated in the system. In the DMPO capture results for the
313 NZVI@ACC/PMS system, the characteristic peaks of DMPO-OH at 1:2:2:1 and
314 DMPO- SO_4 at 1:1:1:1:1 were detected within 2 min, indicating the presence of $\cdot\text{OH}$
315 and $\text{SO}_4^{\cdot-}$ in the reaction system.

316 Theoretical calculations were performed to provide deeper insights into the OII
317 degradation by NZVI@ACC activated PMS. Numerous free radicals were generated
318 in the NZVI@ACC/PMS reaction system. The main types of reactions possible were
319 the free radical reactions and the nucleophilic reactions. The calculations for the local
320 descriptor and Fukui function were performed to identify the most vulnerable sites of
321 OII. The optimized OII molecule is depicted in Fig. 6. The CDD values calculated
322 using Gaussian 09 were listed in Table 1. The highest CDD value of 12 (N) atom
323 indicated that 12 (N) was the site most vulnerable to the attack of oxidative species.
324 The proposed degradation mechanism underlying the reaction for OII degradation by
325 NZVI@ACC/PMS was presented in Fig. 7. First, there reacted a contact among OII,

326 NZVI@ACC, and PMS, and the reaction happened under the action of agitation. Next,
 327 the free radicals produced in the reaction attack the 12 (N), thereby breaking down the
 328 OII structure and producing smaller organic molecules, such as phenyl amine,
 329 naphthalene, etc. Finally, OII was degraded completely into small molecules (CO₂
 330 and H₂O) (Yin, et al., 2017).

331 3.5 Applications

332 Halogen ions are the common anions present in dye wastewater and may react with
 333 SO₄^{·-} and ·OH (Zhang, Parker, 2018) according to the following reaction formula:



335 Here, X denotes the halogen ion, such as Cl⁻, Br⁻, and I⁻.

336 According to the steady-state approximation, the degradation rate of OII may be
 337 expressed as follows:

$$338 \quad R_d = R \times \frac{k_{sub,SO_4^{\cdot-}}[sub]}{k_{sub,SO_4^{\cdot-}}[sub] + k_{X^{\cdot-},SO_4^{\cdot-}}[X^-] + \sum_i k_i[S_i]} + R_{OH} \times \frac{k_{sub,OH}[sub]}{k_{sub,OH}[sub] + k_{X^{\cdot-},OH}[X^-] + \sum_j k_j[S_j]} + R_{SO_5^{\cdot-}} \times \frac{k_{sub,SO_5^{\cdot-}}[sub]}{k_{sub,SO_5^{\cdot-}}[sub] + k_{X^{\cdot-},SO_5^{\cdot-}}[X^-] + \sum_p k_p[S_p]} \quad (6)$$

339 Here, R_d denotes the degradation rate of OII and R_{SO₄^{·-}} denotes the formation rate of
 340 SO₄^{·-} in the reaction. k_{sub,SO₄^{·-}}, k_{sub,OH}, and k_{sub,SO₅^{·-}} are the degradation apparent rate
 341 constants in the substrate. K is the reaction apparent rate constant of the halogen ions.
 342 $\sum k_i[S_i]$ represents the pseudo-first-order reaction rate for SO₄^{·-} with impurities in the
 343 solution.

344 SO₃^{·-} in the solution is rapidly oxidized by O₂ into SO₅^{·-}, the oxidation of which is
 345 quite weak. Moreover, it is difficult to oxidize the halogen ions. Although the
 346 oxidation effect of SO₃^{·-} on OII could be ignored, equation (6) may be reversed to
 347 obtain the following form:

$$348 \quad \frac{1}{R_d} = a + b[X^-] \quad (7)$$

349 It is clear that 1/R_d has a linear relationship with [X⁻]. The fitting results were
 350 presented in Fig. 8 (a)-(c).

351 As depicted in Fig. 8 (a) - (c), the degradation rate of OII decreased rapidly with the
 352 increase in the halogen ion concentration. The degradation rate of OII decreased to
 353 0.053 L/mol·s when the concentration of I⁻ in the solution was increased to 2.0
 354 mmol/L. When the concentration of Br⁻ in the solution was increased to 10 mmol/L,
 355 the degradation rate of OII decreased to 0.113 L/mol·s. When the concentration of Cl⁻
 356 in the solution was increased to 1.0 mol/L, the degradation rate of OII decreased to
 357 0.112 L/mol·s. According to these data, it could be concluded that halogen ions

358 exerted an evident inhibition effect on the OII degradation by the NZVI@ACC/PMS
359 system, and the inhibition effect followed the order: $I^- > Br^- > Cl^-$.

360 Since the addition of the halogen ions reduced the OII degradation efficiency of the
361 NZVI@ACC/PMS system, it was inferred that in the NZVI@ACC/PMS OII
362 degradation system, halogen ions competed for active radicals with the substrates and
363 degradation intermediates, for electron transfer with $SO_4^{\cdot-}$, $\cdot OH$, $SO_5^{\cdot-}$, and $SO^{\cdot-}$, and
364 for other active radicals, resulting in the formation of less active radicals.

365 Owing to the variety of dyes available and the complexity of the actual dye
366 composition, the degradation experiments were conducted using different cationic and
367 anion dyes to evaluate the treatment effect of the NZVIA@ACC/PMS system. The
368 results were presented in Fig. 8 (d). The rates of degradation of CR, OII, RB, and MB
369 at 100 mg/L achieved by the optimal dosage of the NZVI@ACC/PMS system within
370 14 min were 99.39%, 98.32%, 64.61%, and 52.55% under, respectively. It could be
371 observed that the removal rate achieved by the NZVI@ACC/PMS system for anionic
372 dyes was significantly higher than that achieved by this system for cationic dyes,
373 which might be because the anionic dyes assisted NZVI@ACC in generating Fe^{2+} and
374 promoting the generation of active free radicals such as $SO_4^{\cdot-}$.

375 **4. Conclusions**

376 NZVI@ACC was successfully synthesized, and it was revealed that NZVI
377 combined with ACC through coordination bonding, thereby forming a stable structure.
378 NZVI@ACC exhibited high efficiency in activating PMS to degrade OII. The rate of
379 OII degradation (100 mg/L) achieved using the NZVI@ACC/PMS system reached
380 98.32% within 14 min. The reaction system produced a mass of $SO_4^{\cdot-}$, which attacked
381 the 12 (N) of OII, thereby destroying and degrading the structure of OII. Since the
382 NZVI@ACC used in the present study was prepared using ACC from Chaohu
383 cyanobacteria and NZVI, it allows realizing the effective utilization of the
384 cyanobacteria reserves and NZVI.

385

386 **Authors' contributions:**

387 Jun Chen: validation, investigation, visualization, resources, writing, review & editing.

388 Layun Zhu: investigation, methodology, visualization, writing-original draft, writing-
389 review & editing.

390 Sisi Cao: validation, visualization, investigation, review & editing.

391 Zhaoming Chen: investigation, review & editing.
392 Zihui Song: investigation, review & editing.
393 Xiaohong Yang: investigation, review & editing.
394 Jie Jin: validation, resources, writing, review & editing.
395 **Funding:** This research was supported by the National Key R&D Program of China
396 (2020YFC1908601, 2020YFC1908602). Science Development Fund Project of Hefei
397 University (22040521004).

398 **Data availability:** The datasets used and/or analyzed during the current study are
399 available from the corresponding author on reasonable request.

400 **Compliance with ethical standards:**

401 **Ethics approval and consent to participate:** Not applicable.

402 **Consent for publication:** Not applicable.

403 **Competing interest:** The authors declare that they have no competing interest.

404

405 **References**

406 Anipsitakis, G.P., & Dionysiou, D.D. (2004). Radical generation by the interaction of
407 transition metals with common oxidants. *Environmental Science & Technology*,
408 38(13), 3705-3712.

409 Czech, B., Oleszczuk, P., Wiacke A.E., & Barczak, M. (2015). Water treatment by
410 H₂O₂ and /or UV affects carbon nanotube (CNT) properties and fate in water and
411 tanic acid solution. *Environmental Science and Pollution Research*, 22(24),
412 20198-20206.

413 Du, J., Bao, J., Lu, C., & Werner, D. (2016). Reductive sequestration of chromate by
414 hierarchical FeS@Fe(0) particles. *Water Research*, 102, 73-81.

415 Dong, Z.Y., Zhang, Q., Chen, B.Y., & Hong, J.M. (2019). Oxidation of bisphenol A
416 by persulfate via Fe₃O₄- α -MnO₂ nanoflower-like catalyst: Mechanism and
417 efficiency. *Chemical Engineering Journal*, 357, 337-347.

418 Fuller, S.J., Stewart, D.I., & Burke, I.T. (2013). Chromate reduction in highly alkaline
419 groundwater by zerovalent iron: Implications for its use in a permrable reactive
420 barrier. *Industrial & Engineering Chemistry Research*, 52(13), 4704-4714.

421 Gong, Y., Li, D., Luo, C., Fu, Q., & Pan, C. (2017). Highly porous graphitic biomass
422 carbon as advanced electrode materials for supercapacitors. *Green Chemistry*,
423 19(17), 4132-4140.

424 Gao, J., Han, D., Xu, Y., Liu, Y., & Shang, J. (2019). Persulfate activation by sulfide-
425 modified nanoscale iron supported by biochar (S-nZVI/BC) for degradation of
426 ciprofloxacin. *Separation and Purification Technology*, 235, 116202.

427 Hori, H., Yamamoto, A., Hayakawa, E., Taniyasu, S., Yamashita, A., Kutsuna, S.,
428 Kiatagawa, H., Arakawa, R. (2005). Efficient decomposition of environmentally
429 persistent perfluorocarboxylic acids by use of persulfate as a photochemical
430 oxidant. *Environmental Science & Technology*, 39(7), 2383-2388.

431 Hussain, I., Li, M., Zhang, Y., Li, Y., Huang, S., Du, X., Liu, G., Hayat, W., Anwar,
432 N. (2017). Insights into the mechanism of persulfate activation with nZVI/BC
433 nanocomposite for the degradation of nonylphenol. *Chemical Engineering Journal*,
434 311, 163-172.

435 Huang, Z.F., Bao, H.W., Yao, Y.Y., & Lu, W.Y. (2014). Novel green activation
436 processes and mechanism of peroxymonosulfate based on supported cobalt
437 phthalocyanine catalyst. *Applied Catalysis B: Environmental*, 154-155, 36-43.

438 Kwon, M., Kim, S., Yoon, Y., Jung, Y., Hwang, T.M., Lee, J., Kang, J.W. (2015).
439 Comparative evaluation of ibuprofen removal by UV/H₂O₂ and UV/S₂O₈²⁻
440 processes for wastewater treatment. *Chemical Engineering Journal*, 269, 379-390.

441 Lin, Y.T., Liang, C., & Chen, J.H. (2011). Feasibility study of ultraviolet activated
442 persulfate oxidation of phenol. *Chemosphere*, 82(8), 1168-1172.

443 Li, Z., Sun, Y., Yang, Y., Han, Y., & Tsang, D. (2019). Biochar-supported nanoscale
444 zero-valent iron as an efficient catalyst for organic degradation in groundwater.
445 *Journal of Hazardous Materials*, 383, 121240.

446 Lee, J., Gunten, U., & Kim, J.H. (2020). Persulfate-based advanced oxidation: critical
447 assessment of opportunities and roadblocks. *Environmental Science &*
448 *Technology*, 54, 3064-3081.

449 Lian, Y., Han, B., Liu, D., Wang, Y., & Du, Y. (2020). Solvent-free synthesis of
450 ultrafine tungsten carbide nanoparticles-decorated carbon nanosheets for
451 microwave absorption. *Nano-Micro Letters*, 12(1), 153-166.

452 Liu, C., Wang, Y., Zhang, Y.P., Zhang, Y.T., Li, R.Y., Meng, W.D., Song, Z.L., Qi,
453 F., Xu, B.B., Chu, W., Yuan, D.H. (2018). Enhancement of Fe@porous carbon
454 to be an efficient mediator for peroxymonosulfate activation for oxidation of
455 organic contaminants: Incorporation NH₂-group into structure of its MOF
456 precursor. *Chemical Engineering Journal*, 354, 835-848.

457 Li, X.N., Wang, Z.H., Zhang, B., Rykov, A.I., Athemed, M.A., & Wang, J.H. (2016).
458 $\text{Fe}_x\text{Co}_{3-x}\text{O}_4$ nanocages derived from nanoscale metal-organic frameworks for
459 removal of bisphenol A by activation of peroxymonosulfate. *Applied Catalysis B:*
460 *Environmental*, 181, 788-799.

461 Lin, C.C., Lee, Li. T., & Hsu, L.J. (2013). Performance of $\text{UV}/\text{S}_2\text{O}_8^{2-}$ process in
462 degradating polyvinyl alcohol in aqueous solutions. *Journal of Photochemistry*
463 *and Photobiology A: Chemistry*, 252(1), 1-7.

464 Ma, W., Wang, N., Tong, T., Zhang, L., Lin, K., Han, X., & Du, Y. (2018). Nitrogen,
465 phosphorus, and sulfur tri-doped hollow carbon shells derived from ZIF-
466 67@poly (cyclotriphosphazene-co-4,4'-sulfonyldiphenol) as a robust catalyst of
467 peroxymonosulfate activation for degradation of bisphenol A. *Carbon*, 137, 291-
468 303.

469 Pham, H.T., Suto, K., & Inoue, C. (2009). Trichloroethylene transformation in aerobic
470 pyrite suspension: pathways and kinetic modeling. *Environmental Science &*
471 *Technology*, 43(17), 6744-6749.

472 Sun, Y., Cho, D.W., Graham, N., Hou, D., Yip, A., & Khan, E. (2019). Degradation
473 of antibiotics by modified vacuum-UV based processes: Mechanistic
474 consequences of H_2O_2 and $\text{K}_2\text{S}_2\text{O}_8$ in the presence of halide ions. *Science of the*
475 *Total Environment*, 664, 312-321.

476 Sun, Y.M., Song, H., Ma, W.J., Yu, B.Y., & Hu, J.L. (2017). Advanced treatment of
477 penicillin wastewater using Fenton oxidation method. *Fine and Specialty*
478 *Chemical*, 25(2), 23-27.

479 Soubh, A., & Mokhtarani, N. (2016). The post treatment of composting leachate with
480 a combination of ozone and persulfate oxidation processes. *RSC Advances*,
481 6(80), 1-22 .

482 Song, S.J., Ma, F.W., Wu, G., Ma, D., Geng, W.D., & Wan, J.F. (2015). Facile self-
483 template large scale preparation of biomass-derived 3D hierarchical porous
484 carbon for advanced supercapacitors. *Journal of Material Chemistry*, 3(35),
485 18154-18162.13

486 Tsai, T.T., Kao, C.M., Yeh, T.Y., & Lee, M.S. (2008). Chemical Oxidation of
487 Chlorinated Solvents in Contaminated Groundwater: Review. *Practice Periodical*
488 *of Hazardous Toxic & Radioactive Waste Management*, 12(2), 116-126.

489 Wang, D. Z., Jiang, H.M. (2017). Removing the chroma of dye wastewater by Fenton
490 reagent oxidation process. *Industrial Catalysis*, 25(11), 82-84.

491 Wu, Y., Chen, Y., Wang, H., Wang, C., Wang, A., Shuai, Z., Li, X., Sun, D., Jiang, J.
492 (2018). Efficient ORR electrocatalytic activity of peanut shell-based graphitic
493 carbon microstructures. *Journal of Material Chemistry*, 6, 12018-12028.

494 Xu, J., Avellan, A., Li, H., Liu, X., & Lowry, G. V. (2020). Sulfur loading and
495 speciation control the hydrophobicity, electron transfer, reactivity, and selectivity
496 of sulfidized nanoscale zerovalent iron. *Advanced Materials*, 32, 201906910.

497 Yang, S.Y., Yang, X., Shao, X.T., Niu, R., & Wang, L.L. (2011). Activated carbon
498 catalyzed persulfate oxidation of azo dye acid orange 7 at ambient temperature.
499 *Journal of Hazardous Materials*, 186(1), 659-666.

500 Yan, J.C., Chen, M.F., Gao, W.G., Xue, S., & Han, L. (2015). Biochar supported
501 nanoscale zerovalent iron composite used as persulfate activator for removing
502 trichloroethylene. *Bioresource Technology*, 175, 269-274.

503 Yin R, Guo W, Du J, Zhou, X., Zheng, H., Wu, Q., Chang, J., Ren, N. (2017).
504 Heteroatoms doped graphene for catalytic ozonation of sulfamethoxazole by
505 metal-free catalysis: Performances and mechanisms. *Chemical Engineering*
506 *Journal*, 317, 632-639.

507 Zha, F.G., Yao, D.X., Hu, Y.B., Gao, L.M., & Wang, X.M. (2016). Integration of
508 US/Fe^{2+} and photo-Fenton in sequencing for degradation of landfill leachate.
509 *Water Science & Technology*, 73(2), 260-266.

510 Zhong, Y., Pan, Z., Wang, X., Yang, J., & Li, W. (2019). Hierarchical Co_3O_4 nano-
511 micro arrays featuring superior activity as cathode in a flexible and rechargeable
512 zinc-air battery. *Advanced Science*, 6(11), 1802243.

513 Zhou, D., Zhang, C.B., Yu, Y.T., Li, Z., Wu, F., & Chen, L. (2014). A novel
514 photochemical system of ferrous sulfite complex: Kinetics and mechanisms of
515 rapid decolorization of acid orange 7 in aqueous solutions. *Water Research*, 57,
516 87-95.

517 Zhang, M., Xiao, C.M., Zhang, C., Qi, J.W., & Li, J.S. (2020). Large-scale synthesis
518 of biomass@mof-derived porous carbon/cobalt nanofiber for environmental
519 remediation by advanced oxidation processes. *ACS EST Engineering*, 1, 249-260.

520 Zrinyi, N., & Pham, L.T. (2017). Oxidation of benzoic acid by heat-activated
521 persulfate: Effect of temperature on transformation pathway and product

- 522 distribution. *Water Research*, 120, 43-51.
- 523 Zhang, T.T., Yang, Y.L., Gao, J.F., Li, X., Yu, H.K., Wang, N., Du, P., Yu, R., Li, H.,
524 Fan, X.Y., Zhou, Z.W. (2020). Synergistic degradation of chloramphenicol by
525 ultrasound-enhanced nanoscale zero-valent iron/persulfate treatment. *Separation
526 and Purification Technology*, 240, 116575.
- 527 Zhang, K., & Parker, K.M. (2018). Halogen radical oxidants in natural and engineered
528 aquatic systems. *Environmental Science & Technology*, 52 (17), 9579-9594.

Figures

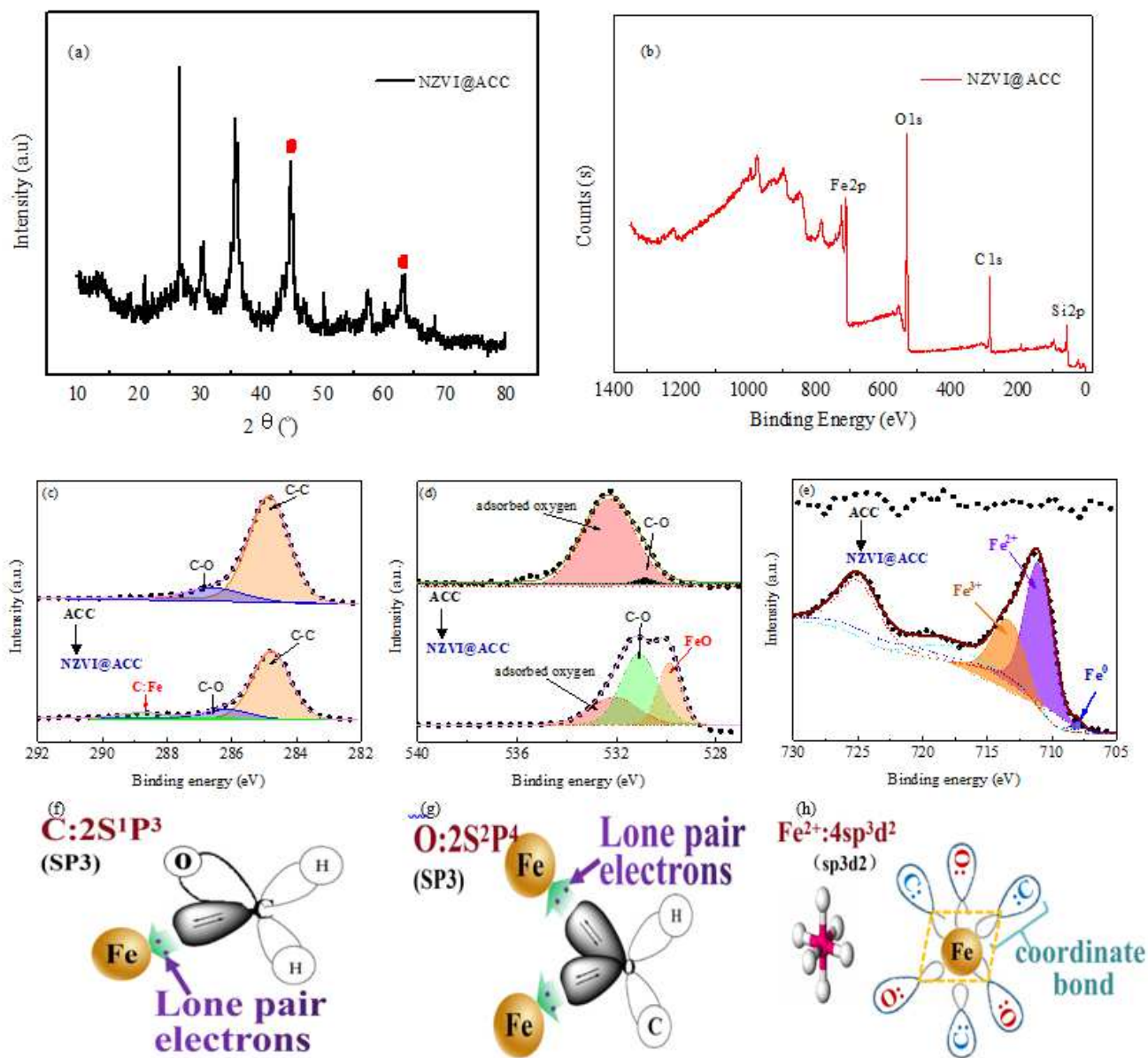


Figure 1

(a) XRD pattern; (b) XPS survey; (c, d, e) Comparative XPS analysis of the C 1s, O 1s, and Fe 2p binding states; and (f, g, h) the mechanism underlying the formation of coordinated bonds in NZVI@ACC.

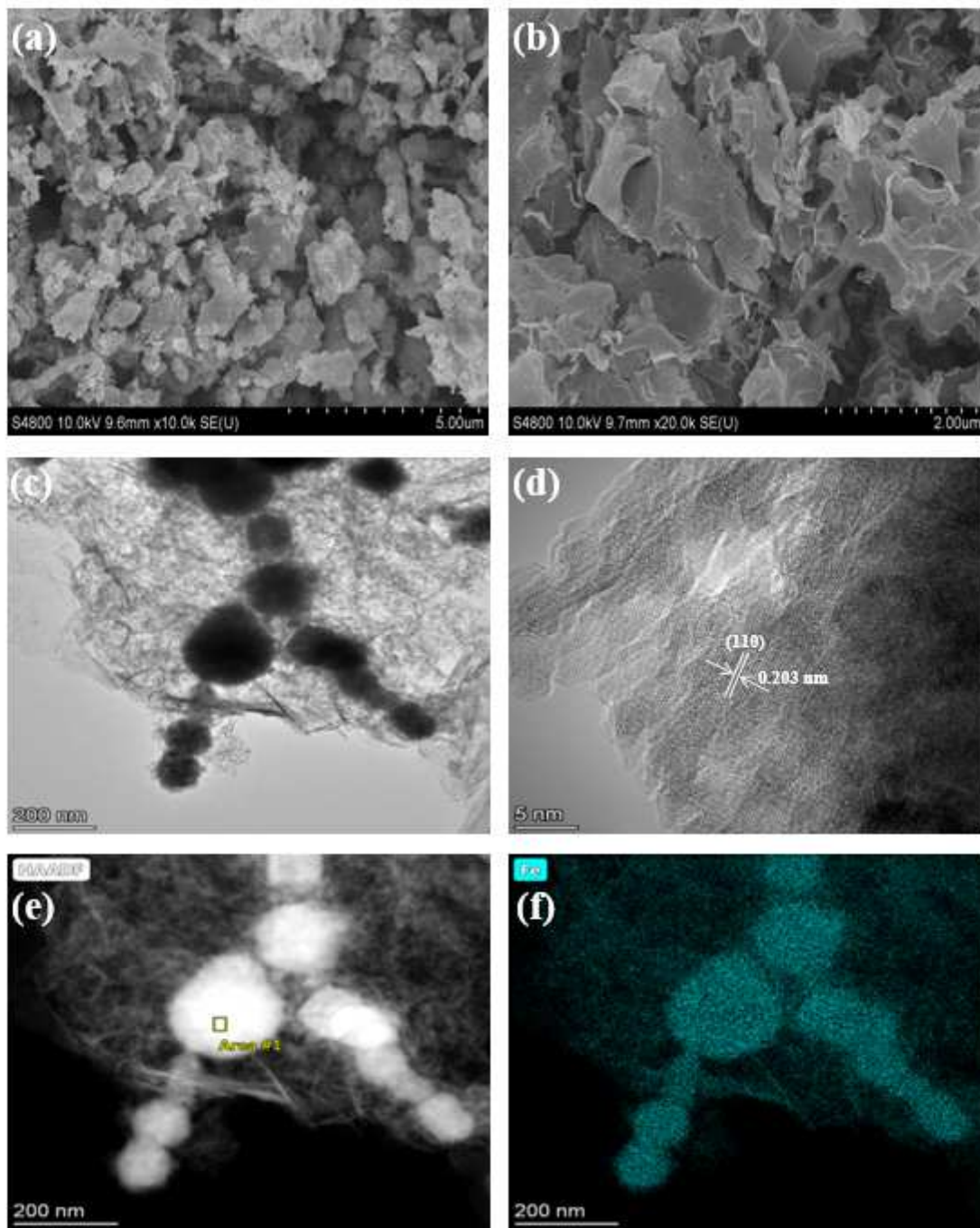


Figure 2

(a, b) SEM; (c, d) TEM; and (e, f) TEM mapping of NZVI@ACC.

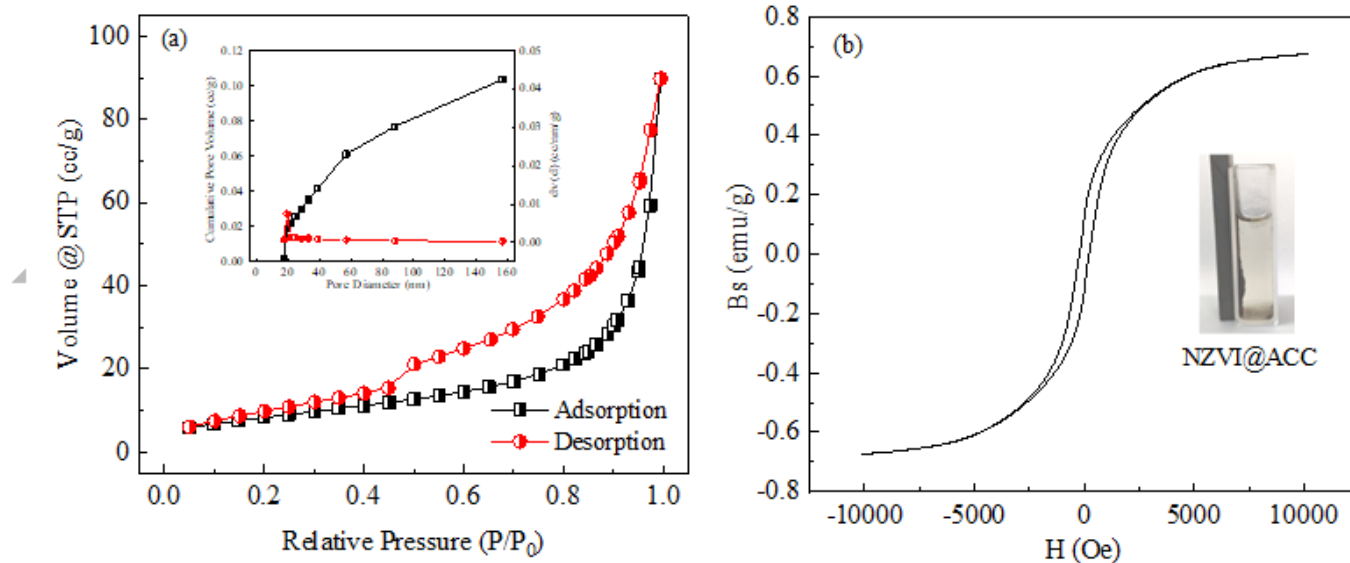


Figure 3

(a) N_2 adsorption-desorption isotherm, and BJH desorption pore size distribution; (b) hysteresis loop of NZVI@ACC, and separation of NZVI@ACC from solution.

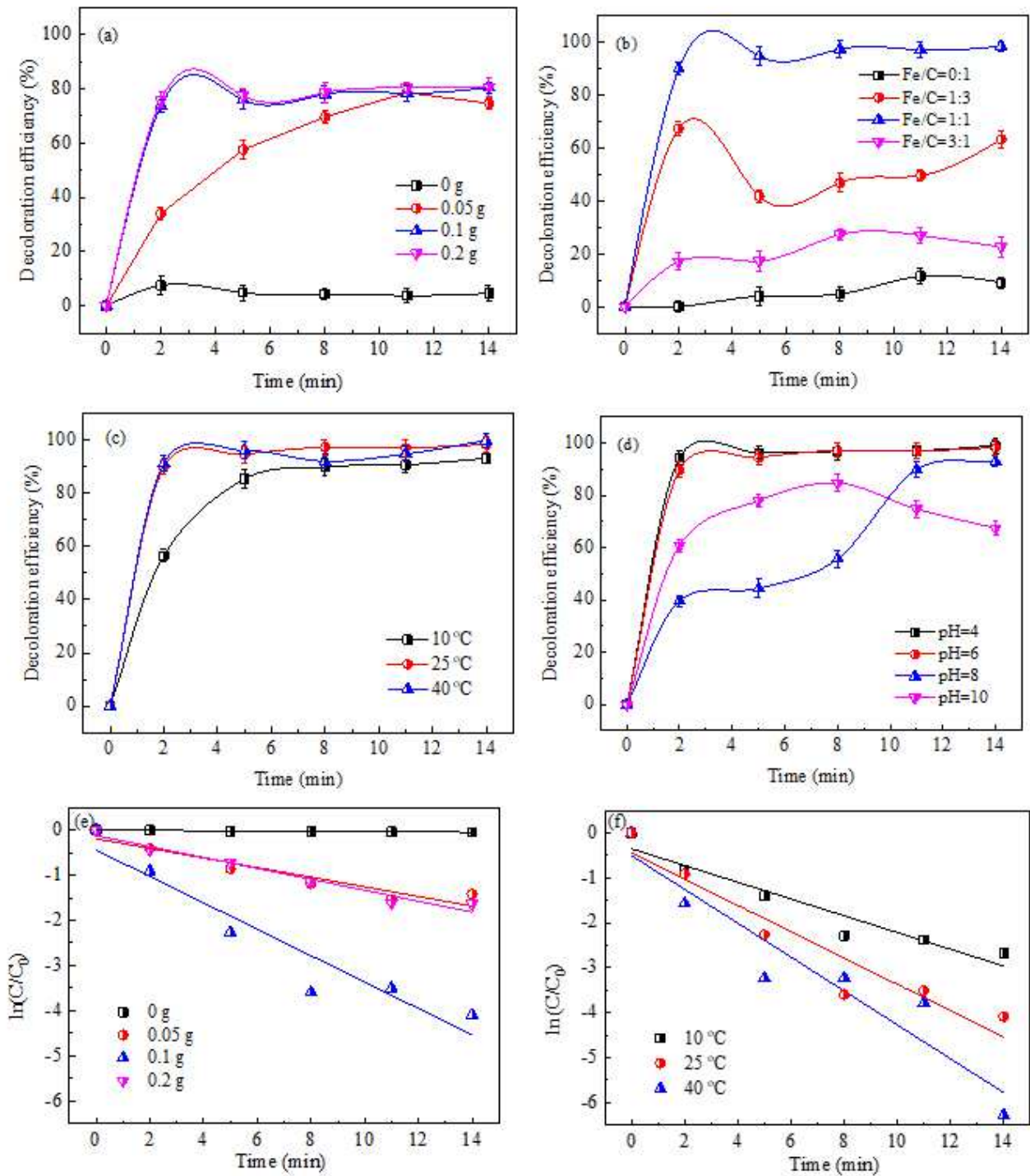


Figure 4

Effect of (a) activator dosage, (b) Fe/C ratio, (c) reaction temperature, (d) initial pH, and kinetic simulation of (e) activator dosage and (f) reaction temperature on OII degradation.

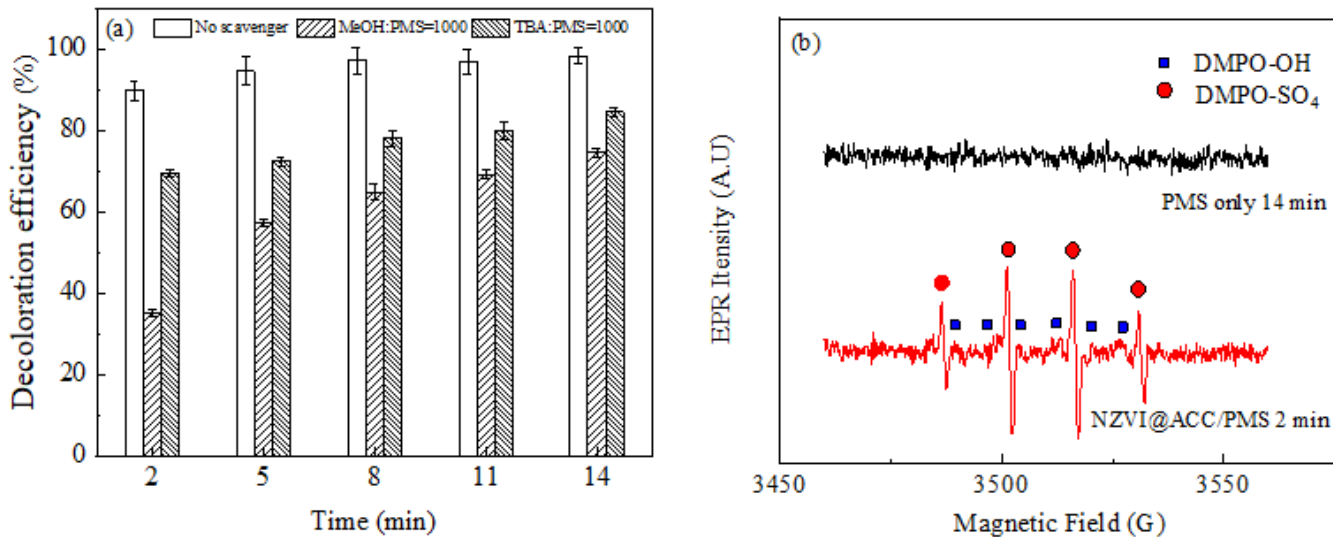


Figure 5

(a) Effects of inhibitors on OII degradation; (b) EPR spectra for DMPO of PMS and NZVI@ACC/PMS.

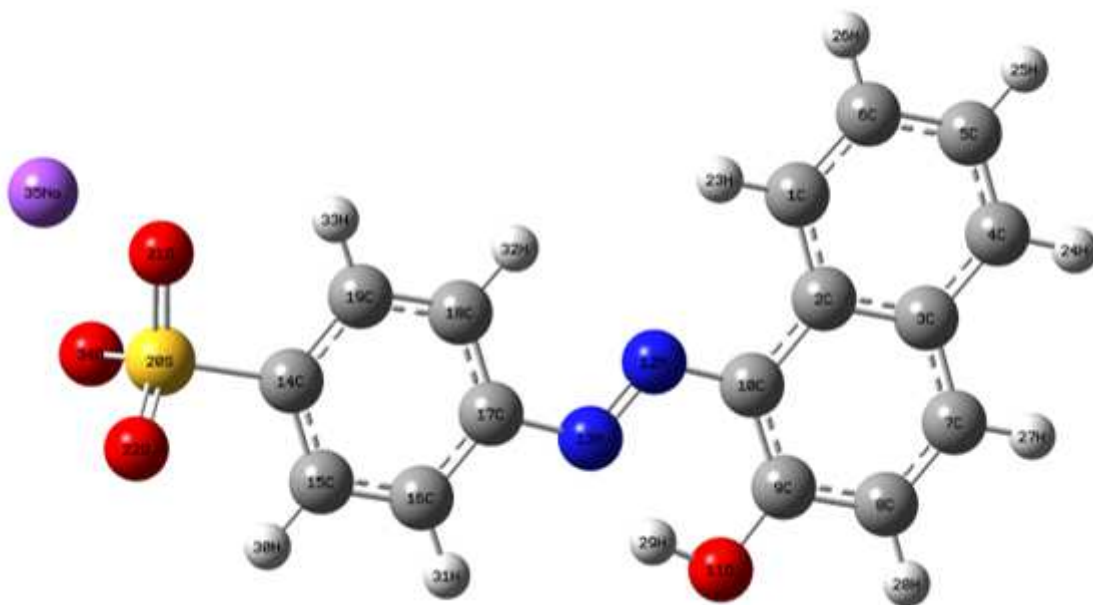


Figure 6

Optimized structure of OII and the numbering system (gray: carbon; red: oxygen; blue: nitrogen; white: hydrogen; yellow: sulfur; and purple: sodium).

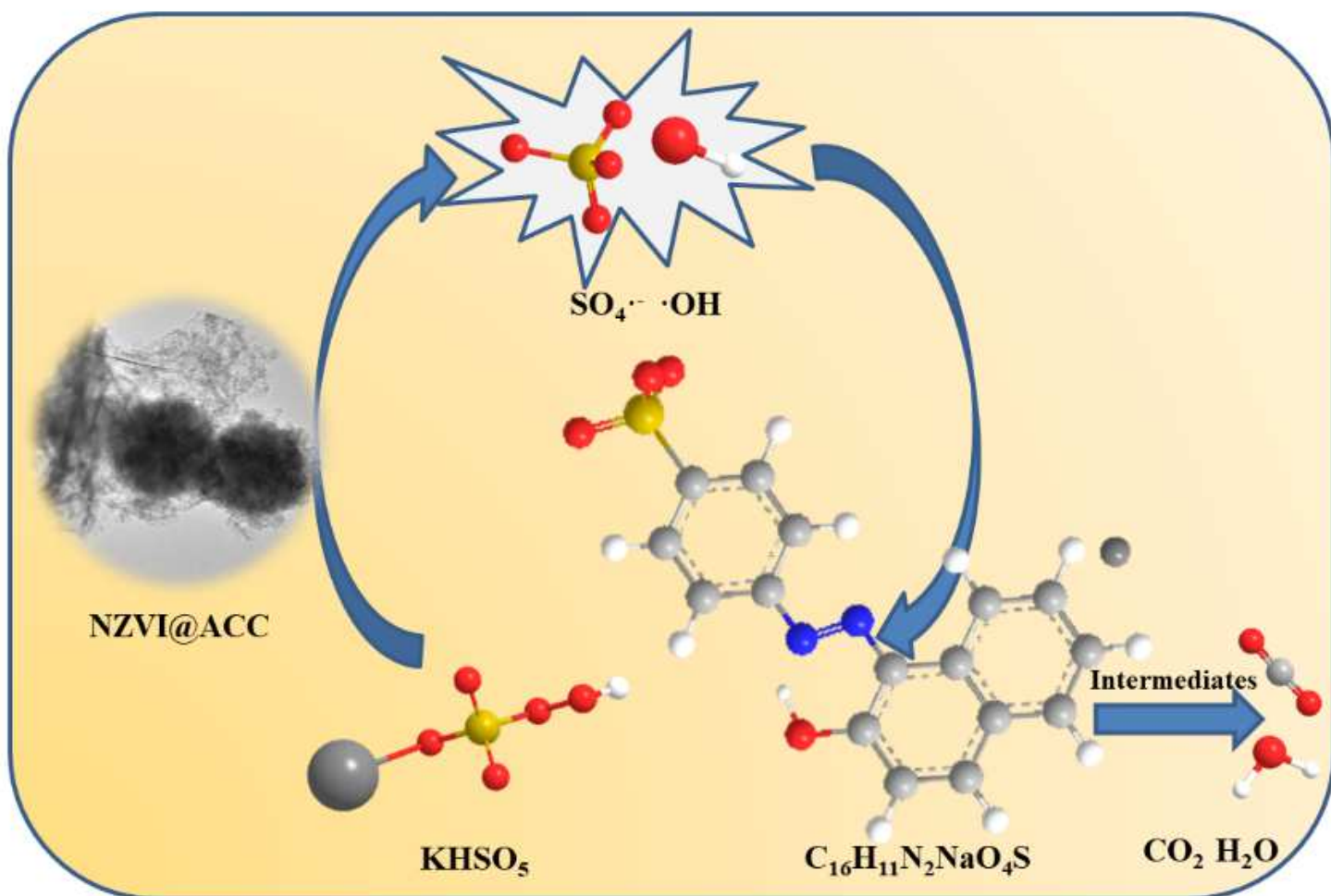


Figure 7

The proposed mechanism underlying the reaction for OII degradation by NZVI@ACC/PMS.

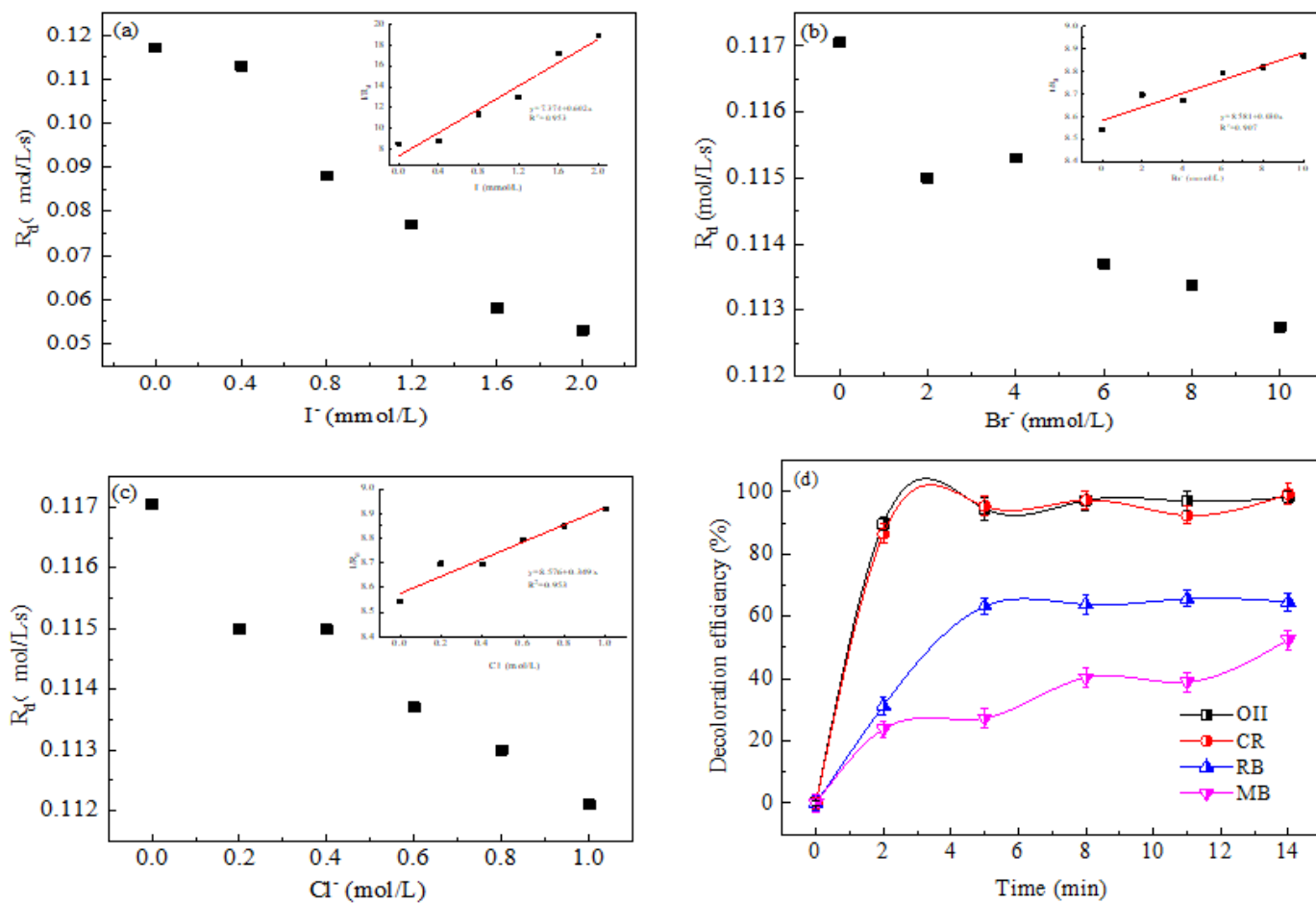


Figure 8

Effect of the NZVI@ACC/PMS system on different (a, b, c) halogens and (d) dyes.